ELSEVIER

Dynamics of Atmospheres and Oceans
36 (2002) 175–200

dynamics of atmospheres and oceans

www.elsevier.com/locate/dynatmoce

The influence of the coast on the dynamics of upwelling fronts Part II. Numerical simulations[1]

Pascale Bouruet-Aubertot*, Vincent Echevin

Laboratoire d'Océanographie Dynamique et Climatologie (LODYC), U. Pierre et Marie Curie, UMR 7617 CNRS/IRD/UPMC, T26 4E Boite 100, 4 Place Jussieu, 75252 Paris Cedex 05, France

Received 12 September 2000; received in revised form 23 January 2002; accepted 25 March 2002

Abstract

We investigated the dynamics of upwelling fronts near a coast. This work was first motivated by laboratory experiments [Bouruet-Aubertot, Linden, Dyn. Atmos. Oceans, 2002] in which the front is produced by the adjustment of a buoyant fluid initially confined within a bottomless cylinder. It was shown that cyclonic eddies consisting of coastal waters are enhanced when the front is unstable near the coast (the outer vertical boundary). The purpose of this paper is to provide further insights into this process. We reproduced the experimental configuration using a three-dimensional model of the primitive equations. We first show that for coastal fronts more potential energy, in terms of the maximum available potential energy, is released than for open-ocean fronts. Therefore, waves of larger amplitude are generated during the adjustment and the mean flow that establishes has a higher kinetic energy in the former case. Then as baroclinic instability starts and wave crests reach the boundary, cyclonic eddies are enhanced as in the laboratory experiments and in a similar way. However, in contrast to the laboratory experiments, offshore advection of cyclonic eddies can occur in two stages, depending on the spatial organization of the baroclinic wave. When the baroclinic wave consists of the sum of different modes and is thus highly asymmetric, the offshore advection of cyclonic eddies occurs just after their enhancement at the boundary, as in the laboratory experiments. By contrast, when a single-mode baroclinic wave develops, neighboring cyclonic eddies first merge before being advected offshore. Very different behavior is observed for open-ocean fronts. First a mixed baroclinic–barotropic instability grows. Then the eddies transfer their energy to the mean flow and the barotropic and baroclinic instabilities start again. An excellent agreement is obtained with the main result obtained in the laboratory experiments: the ratio between growth rates of

* Corresponding author.
E-mail address: pba@lodyc.jussieu.fr (P. Bouruet-Aubertot).

[1] Both authors have contributed equally to this work.

PII: S0377-0265(02)00030-1

surface cyclonic and anticyclonic vorticity increases as the instability develops nearer to the coast.

Keywords: Upwelling fronts; Baroclinic instability; Barotropic instability; Cyclo-geostrophic adjustment

1. Introduction

The understanding of the dynamics of thermohaline fronts in the coastal ocean is very relevant to environmental issues. Indeed fronts may induce or prevent water exchange between the coastal and the deep ocean, depending on their dynamics. Different kinds of fronts may exist in the coastal ocean. Some are due to freshwater discharge from rivers and induce coastal density currents that flow along the coast. For instance, the Ligurian front in the Mediterranean Sea, which forces the North Current (Crépon et al., 1981), provides an illustration of this phenomenon. Others, such as coastal upwelling fronts, are most frequently driven by the wind. When the speed and direction of the wind are favorable, coastal surface waters are driven offshore by Ekman transport and replaced by deep dense water near the coast. In this case, the interface between the light and dense waters rises to the surface and outcrops. When the wind stops, there is dense water near the coast and light water offshore, which constitutes an unbalanced state. There is thus an onshore spreading of light water towards the coast. An along front geostrophic current builds up and eventually becomes unstable under specific dynamical conditions. We here study the dynamical adjustment starting from a static density state, which is close to the oceanic situation after the wind has stopped.

The dynamics of density fronts, either coastal-current or upwelling fronts, have been extensively studied in the laboratory (e.g. Griffiths and Linden, 1981a,b, 1982; Narimousa and Maxworthy, 1985, 1987). Experimentally, these fronts were produced either through the adjustment of a buoyant water parcel or through the continuous release of buoyant fluid. More recently, Verzicco et al. (1997) performed numerical simulations which reproduced the experimental configuration studied by Griffiths and Linden (1981a) and by Holford and Dalziel (1996), consisting in the adjustment of a buoyant water parcel. Essentially these previous studies have shown that the flow evolves into a mixed barotropic–baroclinic instability. The nature of the instability mostly depends on the ratio between the internal radius of deformation of the upper layer and the horizontal scale of the buoyant water (for instance the radius of the buoyant water parcel). The depth ratio between the two layers is the second controlling parameter of the flow. For a small depth ratio the instability is predominantly barotropic, whereas for a greater depth ratio, baroclinic instability dominates.

The question of the influence of the coastal boundary on the dynamics was first addressed by Chia et al. (1982). They described the formation of cyclonic eddies which occur when the baroclinic breaking waves reach the boundary. Quantitative results, based on the analysis of surface vorticity field, were later obtained experimentally by Bouruet-Aubertot and Linden (2002) (hereafter BA&L) who showed that two dimensionless numbers control the evolution of the flow:

- the width, W, of the upwelling region in units of the internal radius of deformation, R_d: $W = (R - R_\mathrm{c})/R_\mathrm{d}$ where $R_\mathrm{d} = \frac{1}{f}[g'h_0]^{1/2}$, R is the radius of the tank of water, and R_c is the radius of the cylinder of buoyant water (see Fig. 1);
- the depth ratio, δ, between the two layers.

They also showed that when W^2 decreases (the front is closer to the coast) and when δ increases (the surface layer is thicker), the growth rate of cyclonic eddies is enhanced compared to that of the anticyclonic vorticity.

The purpose of this paper is to describe the dynamics occurring after the relaxation of the wind forcing at a coastal upwelling and to provide further insights into the asymmetry that results from the presence of the coast. To this end we conducted numerical simulations using a hydrostatic primitive equation model. Several sets of simulations were performed for different values of W^2 and δ.

This paper is organized as follows: we describe in Section 2 the model configuration and the parameterizations used in the simulations; we then introduce the different simulations performed. Section 3 is devoted to the analysis of the results. We first give an overview of the main differences that arise depending on the initial distance between the front and the coast. We then show how the radiation of inertia-gravity waves during the adjustment is modified by the presence of the coast. Next, we describe the front instability and eddy growth. In particular, we determine the nature of the instabilities by analyzing the exchange terms in the eddy kinetic energy budget. We analyze in detail the formation of cyclonic eddies along the coast. The subsequent asymmetry between cyclonic and anticyclonic vorticities is then compared to that obtained in the laboratory experiments (BA&L).

2. Model configuration

2.1. Numerical model and parameterizations

The rigid-lid primitive equations model "Océan Parallélisé" (OPA; (Madec et al., 1998)) is implemented in a configuration as close as possible to the experimental one of BA&L. The model domain is a cylindrical tank of radius R, the total depth is H (Fig. 1). The

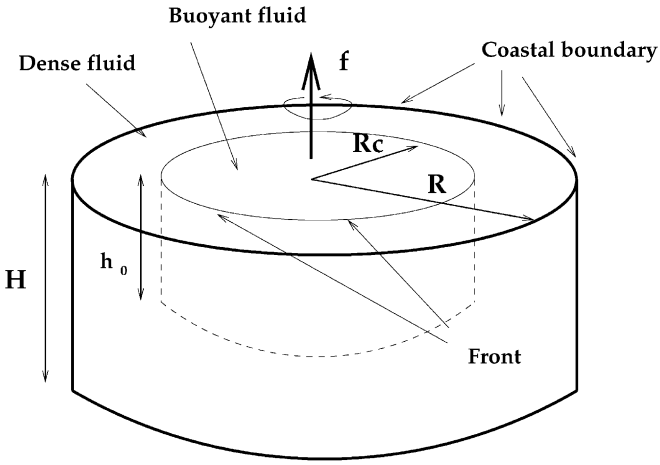

Fig. 1. Model configuration: the domain is a cylinder of radius R, the total depth of water is H while the buoyant fluid is confined within an inner cylinder of radius R_c and height h_0, the Coriolis parameter is denoted by f.

Table 1
Physical and numerical parameters of the simulations

	W^2	δ	H (cm)	h_0 (cm)	$\Delta\rho$ (kg m^{-3})	R (cm)	Δz (cm)	Δt (s)	ν_v
run1.a	32.4	0.43	9.33	4	22.0	46	0.033	0.015	10^{-7}
run1.b	32.4	0.71	9.33	6.67	13.2	46	0.067	0.02	4×10^{-7}
run2.a	13.7	0.43	9.33	4	22.0	37	0.033	0.015	10^{-7}
run2.b	13.7	0.71	9.33	6.67	13.2	37	0.067	0.02	4×10^{-7}
run2.c	13.7	0.71	9.33	6.67	13.2	37	0.067	0.02	4×10^{-7}
run3.a	3.0	0.43	9.33	4	22	28	0.033	0.015	10^{-7}
run3.b	3.0	0.71	9.33	6.67	13.2	28	0.067	0.02	4×10^{-7}
run4.a	1.7	0.43	9.33	4	22.0	26	0.033	0.015	10^{-7}
run4.b	1.7	0.71	9.33	6.67	13.2	26	0.067	0.02	4×10^{-7}
run5	4.0	0.65	13.5	8.8	12.0	37	0.033	0.015	10^{-7}

W^2 is equal to the square of the ratio between the initial distance between the front and the boundary and the radius of deformation of the surface layer, R_d: $W^2 = [(R - R_c)/R_d]^2$, $\delta = h_0/H$ is the depth ratio (see Fig. 1 for definitions of h_0 and H), $\Delta\rho$ is the density difference between the two layers, $f = 2\,\text{rad}\,s^{-1}$ is the Coriolis parameter. R_c is constant, equal to 20 cm, except for run5 in which $R_c = 27$ cm, $R_d = 5$ cm. The horizontal resolution is $\Delta x = \Delta y = 0.5$ cm. For indication in the laboratory experiments, $R = 37$ cm, $R_c = 27$ cm (constant) and R_d varies within the range 1.65–20 cm. Note that the tank in run2.c has a wavy vertical wall of wavenumber 8 in order to test the influence of the curvature upon the development of eddies. Comparisons of our calculations with oceanic flows can be made provided that W^2 and δ are the same.

hydrostatic primitive equations are discretized on a cartesian grid such that the resolution is the same in the x and y horizontal directions and vertical depth levels are regularly spaced. We used a higher vertical resolution for the smallest value of δ (see Table 1). Note that the circular coastal boundary is defined by model grid points $(x(i, j), y(i, j))$ that verify $(x(i, j) - x_0)^2 + (y(i, j) - y_0)^2 = R^2$, with (x_0, y_0) being the horizontal coordinates of the center of the circular domain. Consequently, the boundary of the domain has spatial irregularities of scale equal to the grid size. However, these irregularities do not have any consequences on the flow since the characteristic scale of the eddies (approximating the deformation radius) is much larger than the grid size (see Table 1). This has been checked using a different geometry, that of a periodic channel. Due to the rigid-lid approximation of our model, we have neglected the parabolic shape of the free surface as well as the barotropic surface waves. Regarding the former approximation it is likely that this effect will be negligible within the ranges of our parameters: the ratio between centrifugal acceleration and gravity is small, less than 0.04. We have checked the validity of the latter hypothesis using a specific model configuration with a free surface (Roullet and Madec, 2000). We shall see that neither effect contributes significantly to the dynamics since an excellent agreement is obtained with the laboratory experiments. The so-called Smolarkiewicz scheme is used for the advection of density (Smolarkiewicz and Clark, 1986). Dissipation is modeled for the horizontal velocity components using a biharmonic operator for the horizontal derivatives $(-\nu_h(\partial_x^4 + \partial_y^4))$ and a harmonic operator for the vertical derivative $(\nu_v \partial_z^2)$. The Prandtl number, ν_v/κ, is equal to 1 so that the diffusivity κ is equal to ν_v. Furthermore, a convective adjustment scheme is used to re-establish static stability (Madec et al., 1998). We have tested different kinds of boundary conditions (free-slip, no-slip, linear-friction) along the lateral and bottom boundaries. We did not find any noticeable influence of these boundary

conditions on the results. Here the lateral boundary condition for the horizontal velocity is no-slip and the friction at the bottom boundary is linear.

2.2. Initial state and model parameters

The initial density field is represented in Fig. 1: a cylindrical pool of water of uniform density ρ_0 and depth h_0 is surrounded by denser water of uniform density ρ_1. The outer vertical boundary, $r = R$, is referred to as the coast in the following.

Several simulations were performed for different values of W^2 and δ, the two dimensionless numbers controlling the flow. There are different ways of varying W^2: one can either vary the surface radius of deformation, R_d, or the distance $R - R_\mathrm{c}$. We have chosen here to vary R and hence $R - R_\mathrm{c}$, keeping R_d constant. In this way, the ratio between the characteristic scale of the flow, R_d, and the dissipation scale of our model is constant. Note that the viscosity of the model is taken as small as possible. To check whether our values for the viscosity are consistent with those of the experiments, we first compared the Ekman number. The Ekman number of the lower layer is equal to 2.3×10^{-5} whereas that in the experiments is equal to 6.5×10^{-5}. Since it is difficult to compare Reynolds numbers due to the biharmonic dissipation used in the numerical model we chose to compare values of the maximum vorticity, η. To this aim we have smoothed the numerical data using a window of the same width as that used while processing the experimental data (BA&L, Part I). A good agreement was obtained ($\eta_\mathrm{exp} = 0.66$ and $\eta_\mathrm{num} = 0.80$ for parameters of run5 from Table 1) which shows that the dynamics at the scale of the eddies is well resolved by the numerical model.

We next established a protocol to identify the dominant wavelength and its sensitivity to initial conditions. In the laboratory experiments, this wavelength was inferred from the number of wave crests along the front. However, owing to the asymmetry between the different crests (e.g. Fig. 3 of Part I), the baroclinic wave consisted of a superposition of different azimuthal modes. In the numerical simulations we have considered three cases: an unperturbed density field, as that shown in Fig. 1, a random azimuthal density perturbation and a density perturbation whose wavelength was chosen according to the theoretical value (Griffiths and Linden, 1981a). In all cases, the same dominant wavelength was obtained and was equal to that of the experiments. The only significant difference was that the energy of the azimuthal modes was more widely distributed when a random perturbation was initially introduced. In the following we chose as initial state an azimuthal periodic density perturbation along the front: $R = R_\mathrm{c} + \epsilon \cos(k\theta)$ with $\epsilon = 0.05 R_\mathrm{c}$. The wavenumber k was kept constant, equal to 7, in all simulations having the same $R_\mathrm{c}/R_\mathrm{d}$ value (see Table 1).

3. Results: the influence of the coast on the dynamics

Temporal evolutions of the loss of potential energy, $\mathrm{PE}_\mathrm{loss} = \mathrm{PE}(t = 0) - \mathrm{PE}(t)$, and of kinetic energy, $\mathrm{KE}(t)$, provide an overview of the flow dynamics (Fig. 2). These two quantities are displayed in Fig. 2 which focuses on two cases, that of the most inshore coastal front ($W^2 = 1.7$, Fig. 2a and c) and that of the most offshore open-ocean front ($W^2 = 32.4$, Fig. 2b and d) both having a depth ratio equal to 0.71. Note that the potential energy initially available in the system, $\mathrm{APE}_\mathrm{max}$, depends on the value of W^2 (R differs): $\mathrm{APE}_\mathrm{max} = g(\pi/2)(\Delta\rho/\rho_0)h_0^2 R_\mathrm{c}^2[1-(R_\mathrm{c}/R)^2]$. Therefore, potential energy loss and kinetic

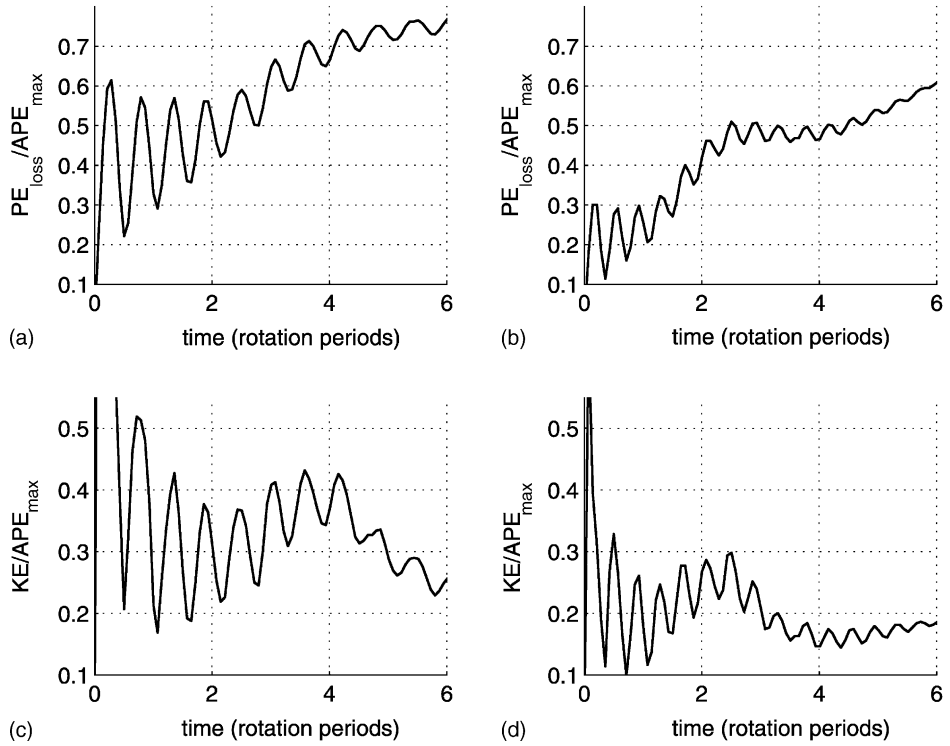

Fig. 2. (a) Potential energy loss, PE_{loss}, normalized by the initial available potential energy, APE_{max}, as a function of time for $W^2 = 1.7$ (coastal front) and $\delta = 0.71$ (run4.b). (b) Same as in (a) but for $W^2 = 32.4$ (open-ocean front) and $\delta = 0.71$ (run1.b). (c) Kinetic energy, KE, normalized by the initial available potential energy, APE_{max}, as a function of time for $W^2 = 1.7$ (coastal front) and $\delta = 0.71$ (run4.b). (d) Same as in (c) but for $W^2 = 32.4$ (open-ocean front) and $\delta = 0.71$ (run1.b).

energy are normalized with APE_{max}. Results obtained for all simulations, namely the four values of W^2 we have considered (within the range 1.7–32.4), are summarized in Table 2.

The dynamics is driven initially by the release of potential energy during the adjustment of the buoyant water parcel. This potential energy loss contributes to the establishment of a mean flow and to the radiation of waves (Fig. 2c and d). A higher release of potential energy is observed for a coastal front (Fig. 2a) than for an open-ocean front (Fig. 2b). When the front develops near the coast this release reaches about $0.6APE_{max}$ (Fig. 2a) whereas this release is only $0.3APE_{max}$ for open-ocean front (Fig. 2b). The reason for the increased potential energy release is investigated further in Section 3.1. As a consequence of this higher potential energy loss, the mean flow that has established just before the front starts to become unstable, has a higher kinetic energy for coastal fronts than for open-ocean fronts. The kinetic energy of the mean flow is about $0.30APE_{max}$ at $t \sim 2$, in the former case (Fig. 2c), and about $0.20APE_{max}$ at $t \sim 1.5$, in the latter case (Fig. 2d). Similarly the energy of the waves generated during the adjustment increases as the front develops closer to the coast. The energy of the waves can be inferred from the amplitude of the oscillating

Table 2
Budget of maximum potential energy loss (PE_{loss}) during the adjustment, maximum of the kinetic energy of the waves and kinetic energy of the mean adjusted flow for all simulations (estimated at the beginning of the front instability)

	W^2	δ	Maximum of PE_{loss} during the adjustment	Maximum of KE of the inertial waves	KE of the mean adjusted flow
run1.a	32.4	0.43	0.40	0.12	0.20
run1.b	32.4	0.71	0.30	0.10	0.20
run2.a	13.7	0.43	0.50	0.15	0.25
run2.b	13.7	0.71	0.35	0.10	0.20
run3.a	3.0	0.43	0.70	0.20	0.30
run3.b	3.0	0.71	0.50	0.15	0.30
run4.a	1.7	0.43	0.80	0.25	0.45
run4.b	1.7	0.71	0.60	0.20	0.30

All quantities are expressed in units of the maximum available potential energy (APE_{max}). Values of W^2 and δ are recalled in the second and the third columns.

component of potential energy loss (Fig. 2a and b) and from the oscillating component of kinetic energy (Fig. 2c and d). The maximum energy of these waves increases from $0.1APE_{max}$ (Fig. 2d) up to about $0.2APE_{max}$ (Fig. 2c). Similarly, for $\delta = 0.43$, potential energy loss increases when W^2 decreases (see Table 2). Note that the maximum value of PE_{loss} for a given W^2 is slightly higher when $\delta = 0.43$ compared to that obtained when $\delta = 0.71$ (see Table 2). Consequently, the energies of the waves and of the mean flow are slightly higher during the adjustment in the former case ($\delta = 0.43$, see Table 2). This difference results from the fact that diffusion, which occurs mainly at the interface, is higher in the cases of the highest values of δ. Consequently, the increase in potential energy associated with this mixing is higher for higher δ and therefore the potential energy loss is smaller for the highest δ value.

Then, the mean potential energy loss increases within the time interval [2; 4.5] (Fig. 2a) and [1.5; 2.5] (Fig. 2b). Meanwhile kinetic energy increases: the gain in kinetic energy during this stage is $\sim 0.15APE_{max}$ (Fig. 2c and d) while the increase in potential energy loss is $\sim 0.25APE_{max}$ (Fig. 2a and b). We shall see (Section 3.2) that this increase corresponds to the onset of baroclinic instability. Eventually potential energy loss weakens as the instability decreases (see Fig. 2a for $t > 4$ and Fig. 2b for t within the range 2.5–4). During this stage, kinetic energy decreases (Fig. 2c for $t > 4$ and Fig. 2d for t within the range 2.5–4). Then, for open-ocean fronts only, there is a small increase in kinetic energy (Fig. 2d for t within the range 4–6). This increase is associated with an increase in PE_{loss} (Fig. 2b for t within the range 4–6) which suggests the restart of baroclinic instability.

Basically two main effects can be inferred from Fig. 2. Firstly, higher release of potential energy takes place during the adjustment of coastal fronts. Secondly, the mean flow that is established and the waves that are generated are more energetic for coastal fronts (see Table 2). In the following subsections we analyze in detail the evolution of the flow.

3.1. Adjustment of the front and radiation of inertia-gravity waves

The front first adjusts to a quasi-equilibrium state by radiating waves in the two-layer region toward the center of the tank ($r < R_c$). During this stage, the dynamics is

axisymmetric. Therefore, we have a clear view of the dynamics in a vertical plane ((r, z) in cylindrical coordinates). To understand why more potential energy is released for a coastal front, we have displayed the density field in a vertical plane during the beginning of the adjustment process. Fig. 3a, c, e and g correspond to a coastal front and Fig. 3b, d, f and h correspond to a open-ocean front. Velocity vectors of components (u_{rad}, w), where u_{rad} is the radial velocity and w is the vertical velocity component, are plotted as well. Since the initial state is not in geostrophic equilibrium, part of the potential energy available is converted into kinetic energy after $t = 0$. Most of the potential energy is released at the periphery of the buoyant water pool. This energy radiates away from the front (see Fig. 3b, d and f), into the stratified area, since no energy can propagate outward ($r > R_{\mathrm{c}}$) due to the homogeneous vertical stratification. Typically, a train of waves propagates toward the center of the tank and reaches the center after about 0.6 rotation period for run1.b (see Fig. 3b, d, f and h). After the first wave front has reached the center it is radiated away from the center back toward the front. Other wave fronts are generated on the inner side of the front. The circular eddy thus pulses between a wide and shallow phase (minimum interface depth, maximum radius), of minimum potential energy, and a narrow and deep phase (maximum interface depth, minimum radius), of maximum potential energy (see Cushman-Roisin et al., 1985). These two phases can be seen in Fig. 3f and h: when potential energy starts to increase from its minimum value (Fig. 3f) the negative horizontal vorticity in the frontal region, $\partial_z u - \partial_r w$, tends to increase the potential energy (see velocity vectors) whereas when potential energy starts to decrease from its maximum value (Fig. 3h) the positive horizontal vorticity tends to decrease the potential energy. The time interval between these two stages is about $T_{\mathrm{i}}/2$ (where T_{i} is the inertial period) and this two-phase process takes place during several rotation periods. Let us now consider the release of potential energy during the first inertial period near the coast. The horizontal vorticity associated with this release is negative as just seen. When the spreading patch hits the coast a downwelling of the buoyant water is induced for mass conservation. In this way, the already negative horizontal vorticity is reinforced. Therefore, the slope of the interface decreases further and the release of potential energy is increased near the coast. As a consequence, radiated inertial gravity waves are more energetic in this case.

We next estimated the group velocity and frequency of the wave packets radiated during the adjustment. The group wave velocity c is computed from Fig. 3: we obtain $c_{\mathrm{num}} \sim 5.39\,\mathrm{cm\,s^{-1}}$ for run2.b and $c_{\mathrm{num}} \sim 5.17\,\mathrm{cm\,s^{-1}}$ for run4.b. This is reasonably close to the group velocity of a plane wave of small wavelength inferred from linear theory: $c_{\mathrm{th}} = \sqrt{g' h_0 (H - h_0)/H} = 6.12\ \mathrm{cm\,s^{-1}}$ with parameters of run2.b and run4.b (see Table 1). However, we did not expect better agreement since mixing occurs at the interface and the

Fig. 3. Density as a function of radius and depth at different times during the adjustment in two cases. The left column (a, c, e and g) corresponds to the case of a coastal front (run4.b), the right column (b, d, f and h) to that of an open-ocean front (run2.b). The full vertical section is represented in (a) and (b) while only one-half of the vertical section is shown in the other figures for better visualization. Note that the horizontal scale is different for the two columns, since the radius of the tank differs ($R = 26\,\mathrm{cm}$ for run2.b and $R = 37\,\mathrm{cm}$ for run4.b). Times, indicated in rotation periods (T), are: (a) and (b) $t = 0.13T$, (c) and (d) $t = 0.19T$, (e) and (f) $t = 0.25T$ (local maximum of $\mathrm{PE_{loss}}$), (g) and (h) $t = 0.50T$ (local minimum of $\mathrm{PE_{loss}}$). The horizontal velocity scale ($\mathrm{m\,s^{-1}}$) is indicated by an arrow near the bottom left corner, density by the gray scale (density increases from light to dark gray) and by isolines from 30 to 42 every $2\,\mathrm{kg\,m^{-3}}$.

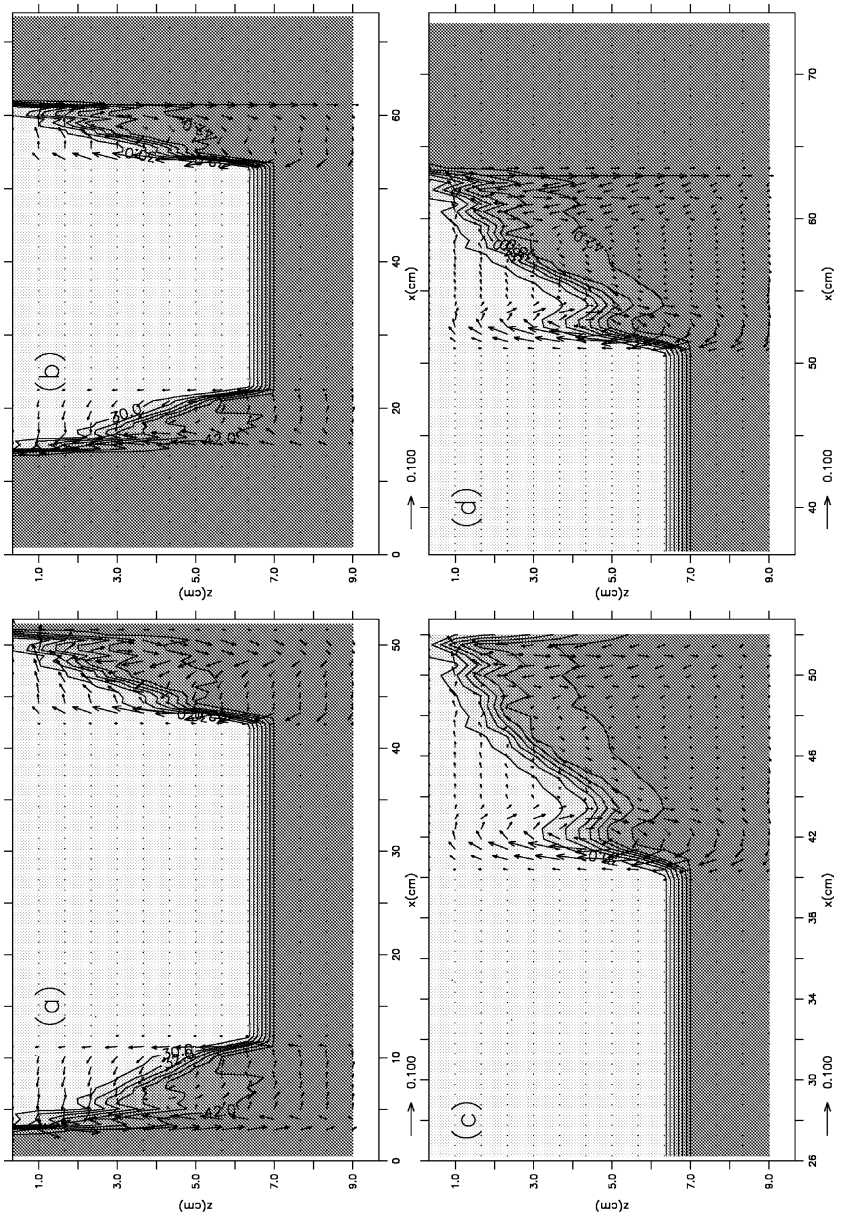
(a)
(b)
(c)
(d)
z(cm)
x(cm)
0.100
1.0
3.0
5.0
7.0
9.0
0
10
20
30
40
50
60
70
26
34
38
42
46

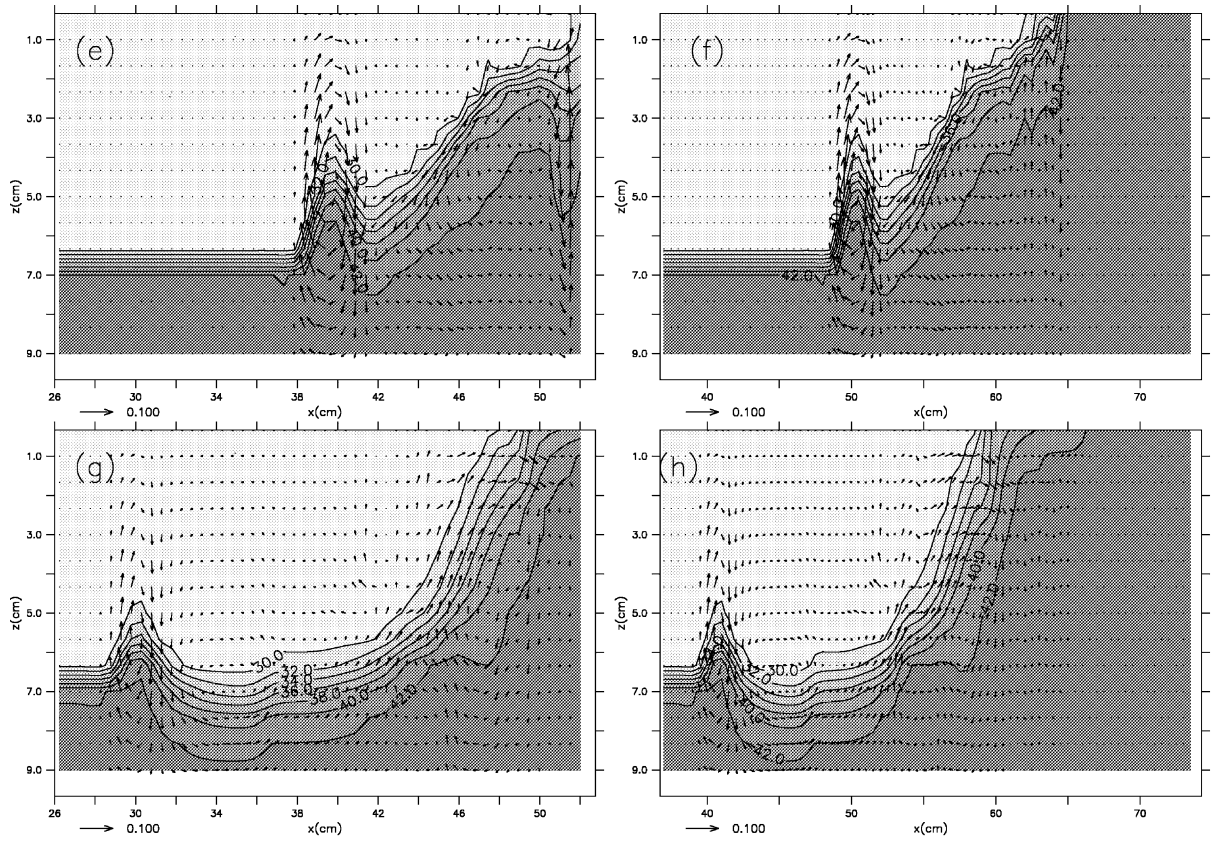

Fig. 3. (*Continued*).

stratification cannot be considered as that of a two-layer fluid. Moreover, linear wave theory may not be valid close to the periphery of the light water, since the thickness of the surface layer h_0 and the vertical displacement of the interface have a similar order of magnitude and since the geometry is cylindrical.

We then estimated the frequency of the radiated gravity waves. In the laboratory experiments (BA&L; Holford, 1994), the frequency of the waves was found to be slightly subinertial, typically within the range $(0.93–0.97)f$. These authors suggested that the frequency was reduced compared to the theoretical value because the waves experienced an effective background rotation smaller than that of the tank due to the anticyclonic motion of the vortex. Our purpose is to find out whether the frequency of the waves is modified by the background anticyclonic motion. To this end we looked at the oscillations of the interface along circles of varying radii (Fig. 4a). The depth of the interface h between the two density layers displays quasi-sinusoidal oscillations at a frequency ω close to the inertial frequency f (Fig. 4a). The amplitude of the oscillations varies with the distance to the center r (Fig. 4a). Oscillations are maximum at the center with an amplitude of $\sim$1 cm and with an initial interface depth at $z = -4$ cm. When r increases, the amplitude of the oscillations first decreases ($r = 20$ cm, Fig. 4a). Then the amplitude increases again in the frontal region ($r = 22$ cm, Fig. 4a). At $r \sim 32$ cm, the isopycnal outcrops. The increase in the energy of the waves near the front suggests that some waves are trapped between the frontal region of negative vorticity and the outer cyclonic boundary of the front. Indeed regions of negative vorticity can trap inertia-gravity waves locally as described by Kunze (1985).

Fast Fourier transforms of $h(r, t)$ time series (Fig. 4b) show a continuum of energy at frequencies around f which is consistent with the classical dispersion relation of inertia-gravity waves ($\omega^2 = f^2 + k^2c^2$, with $c = \sqrt{g'h_0(H - h_0)/H}$; Gill, 1982). In the presence of relative vertical vorticity ζ, the same dispersion relation is valid but with an effective Coriolis parameter f_{eff} equal to $f + (\zeta/2)$ (Kunze, 1985). Near the center, the main frequency peak is at $\omega = 1.2f$ whereas this peak is shifted toward a lower frequency $\omega = 1.0f$ at $r = 22$ cm. This frequency shift is consistent with the fact that near the center of the vortex the relative vertical vorticity ζ is weak while on the inner side of the front ($r \sim 27$ cm) ζ is negative, therefore $f_{\text{eff}} < f$. As a consequence, frequencies $\omega \sim [f_{\text{eff}}^2 + c^2k^2]^{1/2}$ lower than f are excited. The frequency shift inferred from the value of the anticyclonic vorticity in the frontal region is $0.25f$, which is in qualitative agreement with the frequency shift observed in Fig. 4b.

At the end of the adjustment, asymmetric perturbations start to grow and dominate the flow while inertia-gravity waves are dissipated.

3.2. *Instability of the front*

As seen in Part I the onset of baroclinic instability is characterized by the growth of cyclonic vorticity at the surface which is located at the wave crests (see Fig. 10 of Part I). We show in Fig. 5 that the time evolution of the spatially averaged cyclonic and anticyclonic vorticities behaves in a similar way as that observed in the experiments. The growth of cyclonic vorticity starts after about two rotation periods. The instability then saturates after seven rotation periods. Detachments of cyclonic eddies next occur almost at the same time ($t \sim 8T$ and $t \sim 10T$ in Fig. 5) and are characterized by small peaks of the cyclonic vorticity.

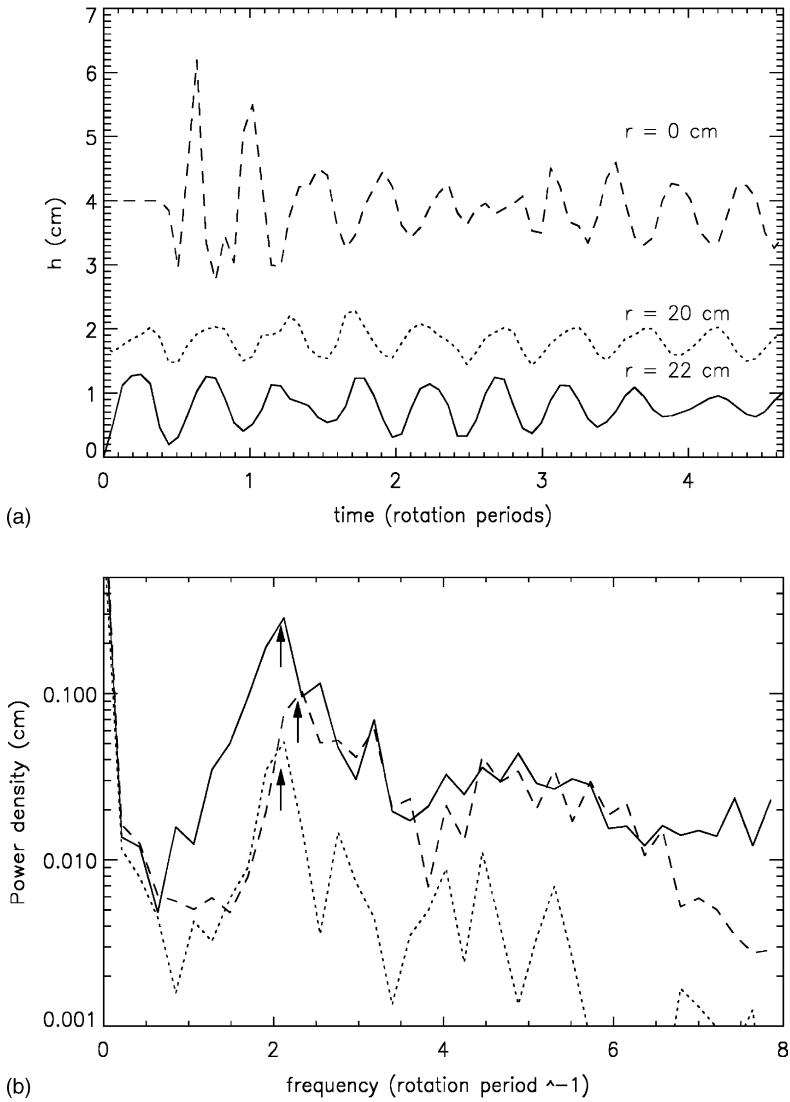

Fig. 4. (a) Temporal evolution of the displacement of the interface between the two layers $h(r,t)$ for different values of radius r (run4.a). (b) Power spectrum of the interface displacement for different values of r: $r = 0$ cm (dashed line), $r = 20$ cm (dotted line), $r = 22$ cm (solid line). Note the frequency shift indicated by arrows.

Figs. 6 and 7 show the temporal evolution of the surface density and velocity fields after the front has started to become unstable. The former corresponds to an open-ocean front and the latter to a coastal front. The associated temporal evolution of energies (eddy kinetic energy, EKE, mean kinetic energy, MKE, and potential energy, PE) and energy-transfer terms for EKE and MKE are displayed in Fig. 8 (see Appendix A for details).

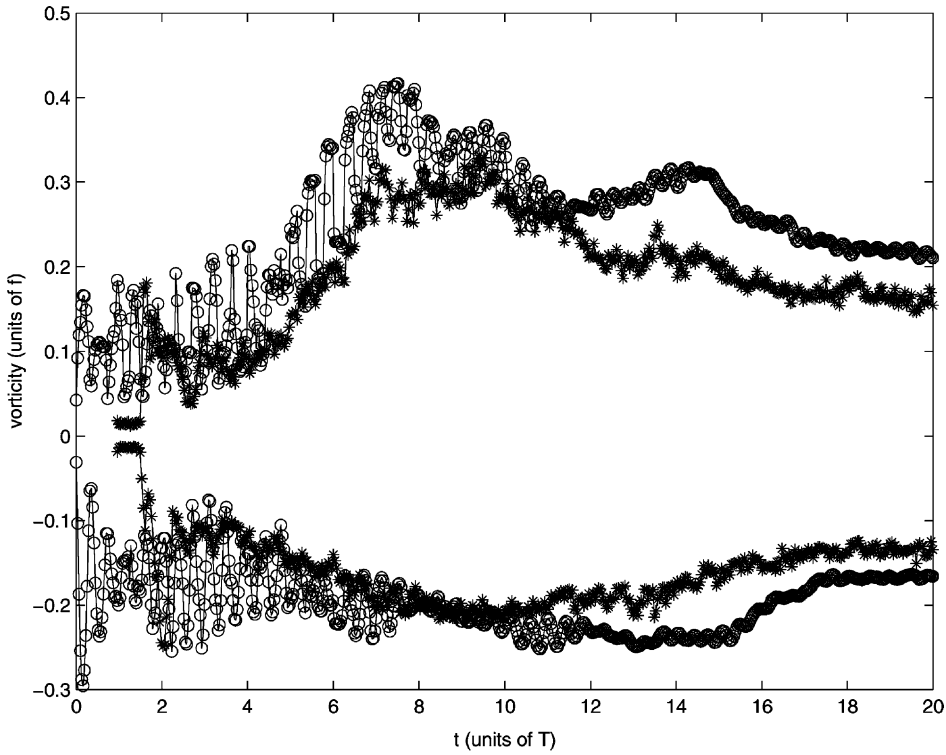

Fig. 5. Time evolution of the cyclonic and anticyclonic vorticities spatially averaged at the surface. The experimental values are represented with black stars while the numerical values are represented with black circles. Note that the vorticity of the numerical simulations has been smoothed using a window of the same width (equal to $1.5R_d$) as that used while processing the experimental data.

The instability takes the form of a mode 7 wave which is growing in amplitude (Figs. 6a and 7a). As indicated by the energy-transfer terms, barotropic and baroclinic processes first come into play (Fig. 8c; $t \sim 1.5$). However, baroclinic instability soon dominates (see the baroclinic term (PE $\rightarrow$ EKE) within the time interval [1.5, 3] in Fig. 8c and d). Baroclinic instability leads to the classical backward-breaking waves (Fig. 6b) whose anticyclonic crests are entrained backward by the cyclonic motion occurring at the wave troughs (e.g. Griffiths and Linden, 1981a). Later, as the wave amplitude increases, closed cyclonic eddies are generated (Fig. 6b and c). Thus, dipoles made of cyclonic eddies and part of the previous anticyclonic wave crests form (Fig. 6c and d). These dipoles then organize themselves in such a way that the cyclonic eddy is on the inner side of the front while the anticyclonic one is on the outer side (Fig. 8d and e). Thus, the inner side of the cyclonic eddies contributes to reinforcing the mean anticyclonic flow (Fig. 6d and e). This increase in the mean flow leads to a fairly regular anticyclonic motion (Fig. 6e), similar to that of the initial adjusted vortex, but of smaller radius. Meanwhile the outer side of the anticyclonic eddies leads to the formation of a mean anticyclonic circulation (Fig. 6e). This process results in energy

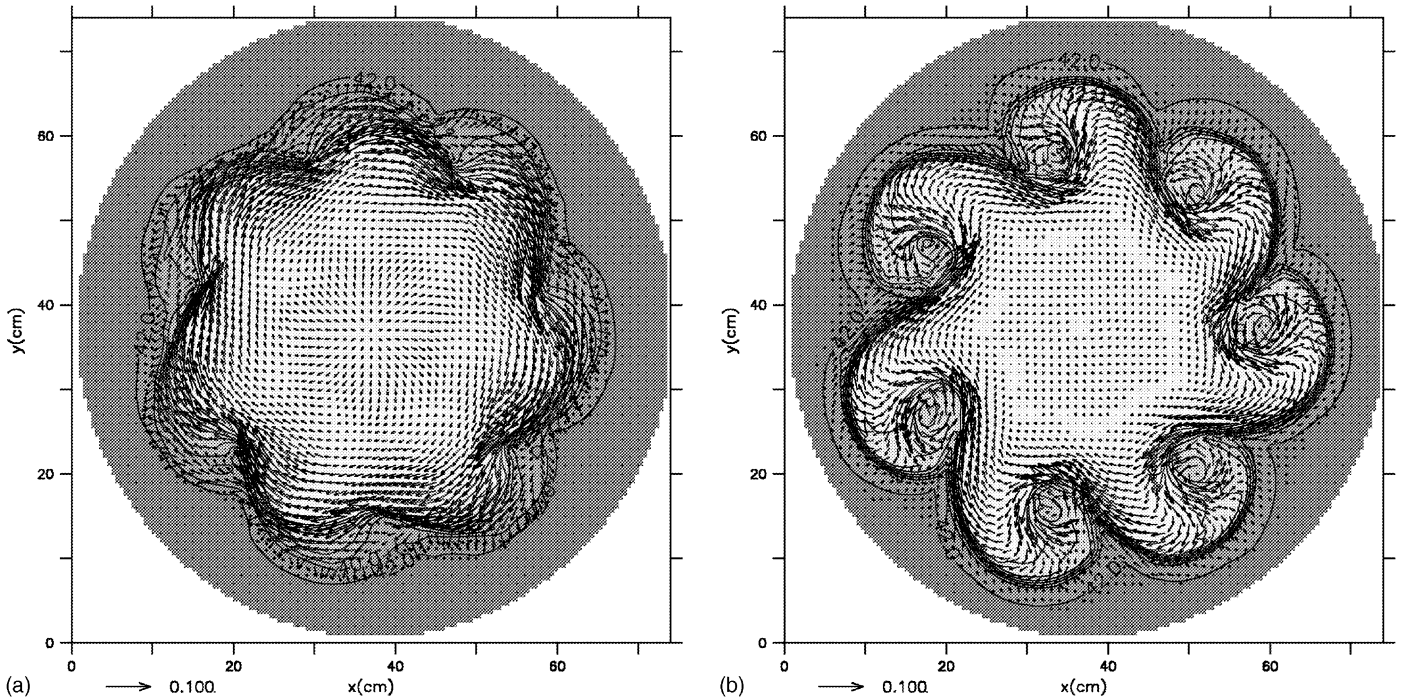

Fig. 6. Surface velocity and density fields at different times (run2.b). Horizontal velocity vectors ($\mathrm{m\,s^{-1}}$) are represented by arrows and density by the gray scale (density increases from light to dark gray) and by isolines from 30 to 42 every $2\,\mathrm{kg\,m^{-3}}$. The horizontal domain is a circle of radius $r = 37\,\mathrm{cm}$ and the buoyant fluid is initially confined horizontally within a circle of radius $r = 20\,\mathrm{cm}$: (a) $t = 1.27T$, (b) $t = 2.55T$, (c) $t = 3.50T$, (d) $t = 3.75T$, (e) $t = 4.84T$, (f) $t = 7.20T$; time is indicated in units of rotation period, T.

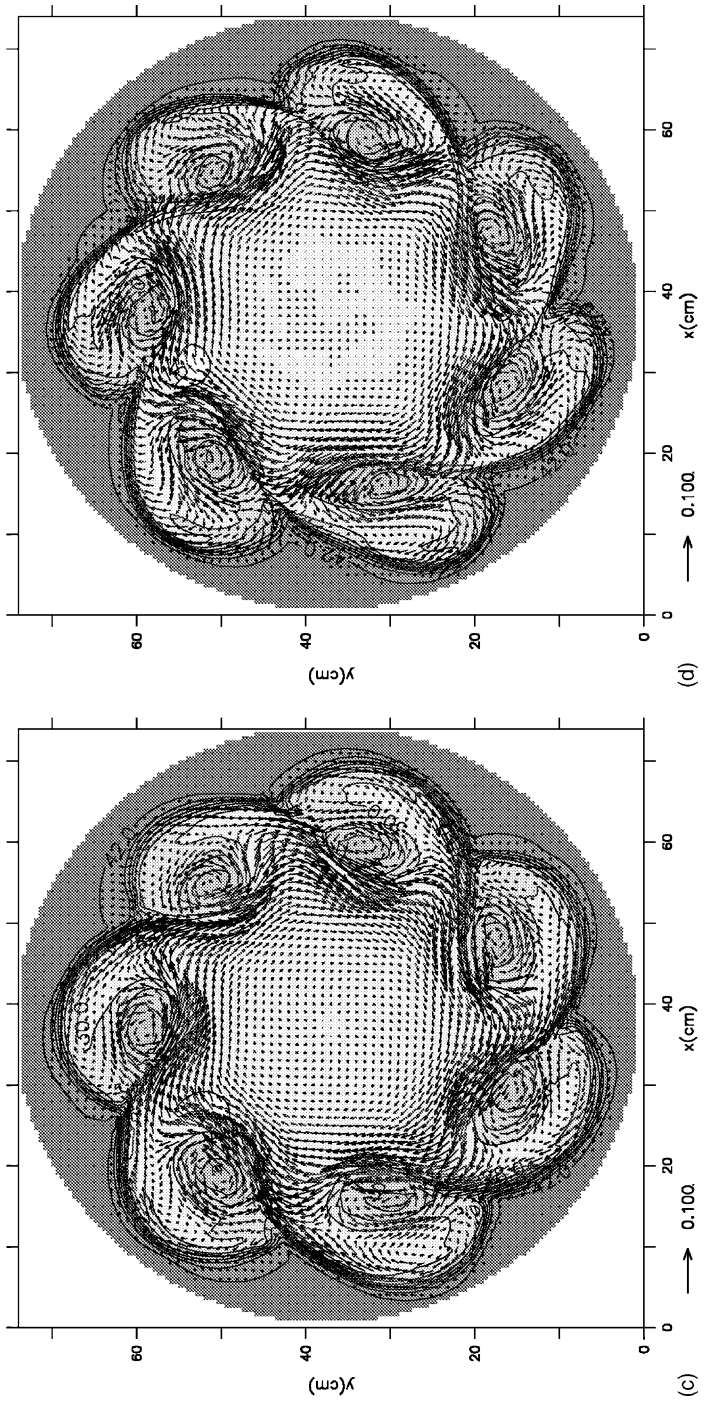

Fig. 6. (*Continued*).

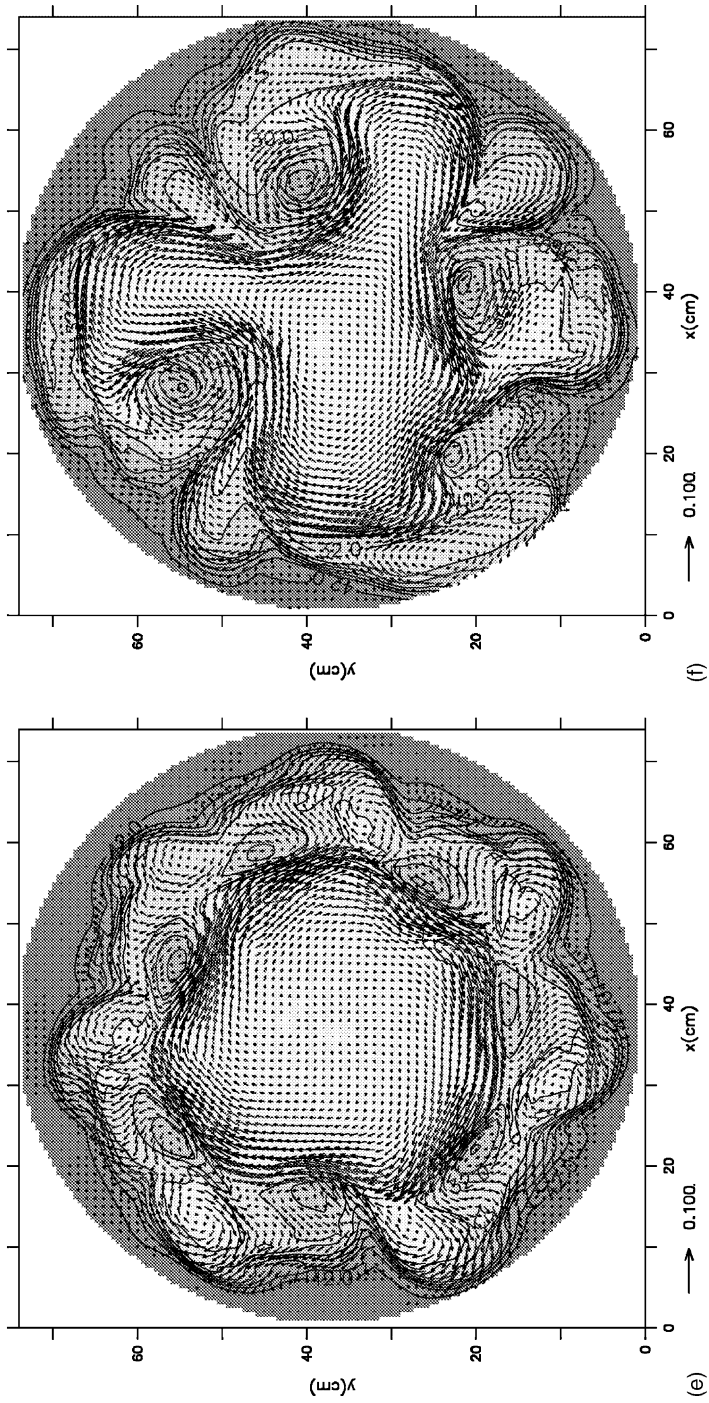

Fig. 6. (*Continued*).

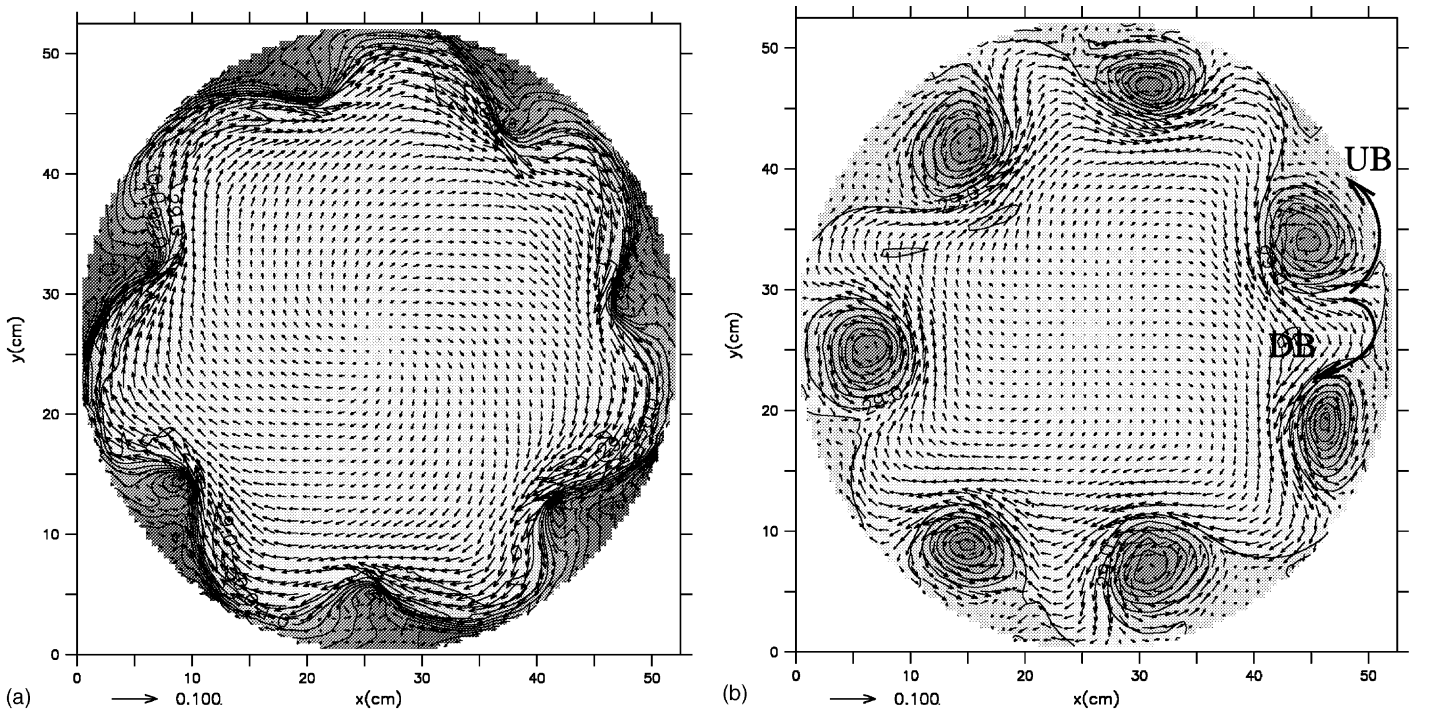

Fig. 7. Surface velocity and density fields at different times for a coastal front run4.b from (a)–(d), and run3.a from (e) and (f). Horizontal velocity vectors ($m\,s^{-1}$) are represented by arrows and density by the gray scale (density increases from light to dark gray) and by isolines from 28 to 44 every $1\,kg\,m^{-3}$ (a–d) and from 30 to 42 every $2\,kg\,m^{-3}$ (e and f). The horizontal domain is a circle of radius $r = 26\,cm$ (a–d) and $r = 28\,cm$ (e and f). The buoyant fluid is initially confined horizontally within a circle of radius $r = 20\,cm$: (a) $t = 2.23T$, (b) $t = 4.77T$, (c) $t = 6.75T$, (d) $t = 8.92T$, (e) $t = 4.84T$, (f): $t = 8.09T$; time is indicated in units of rotation period, T.

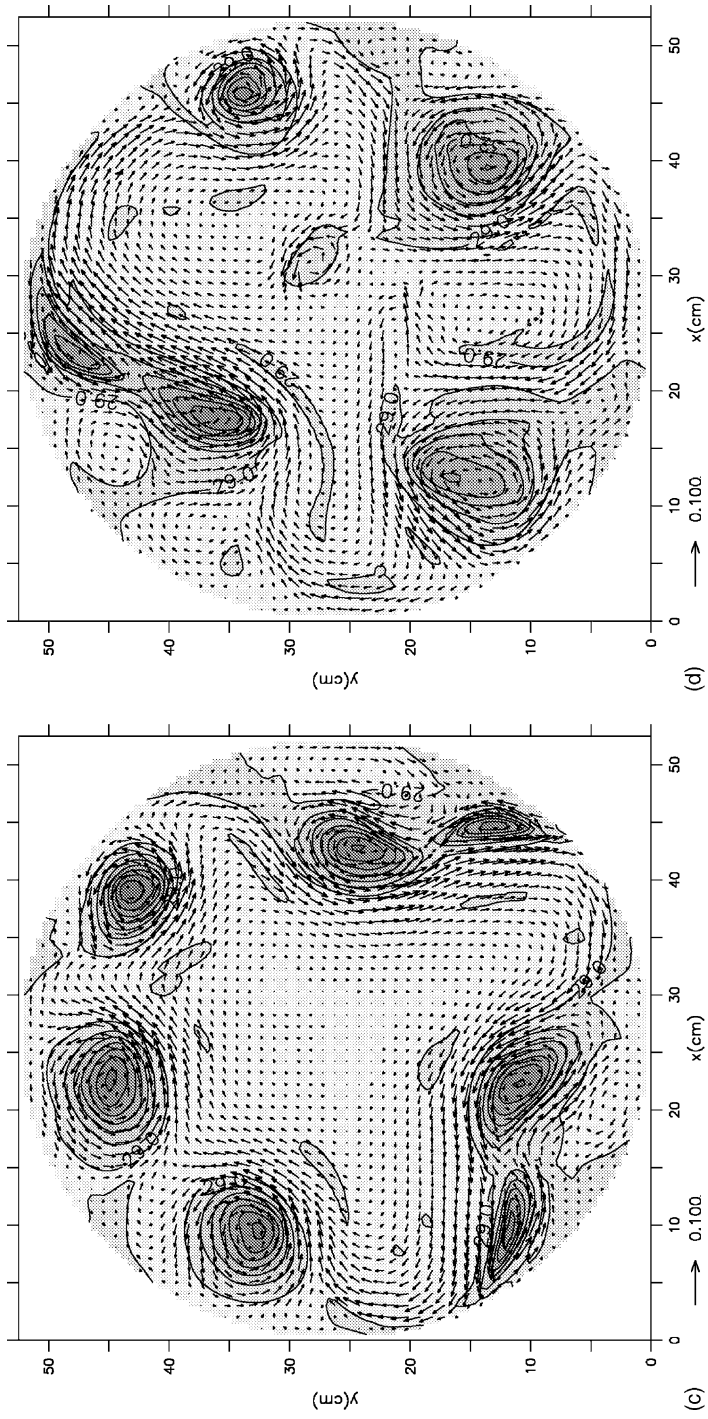

Fig. 7. (*Continued*).

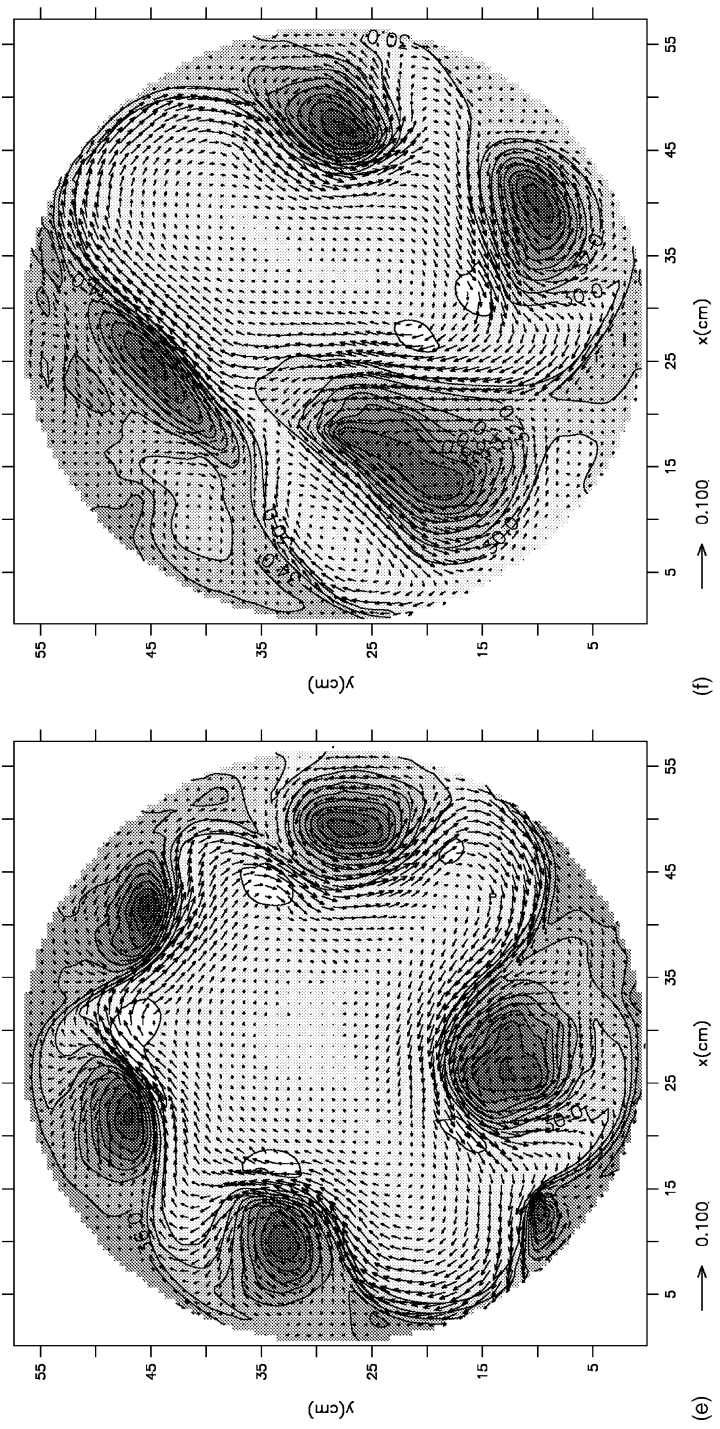

Fig. 7. (*Continued*).

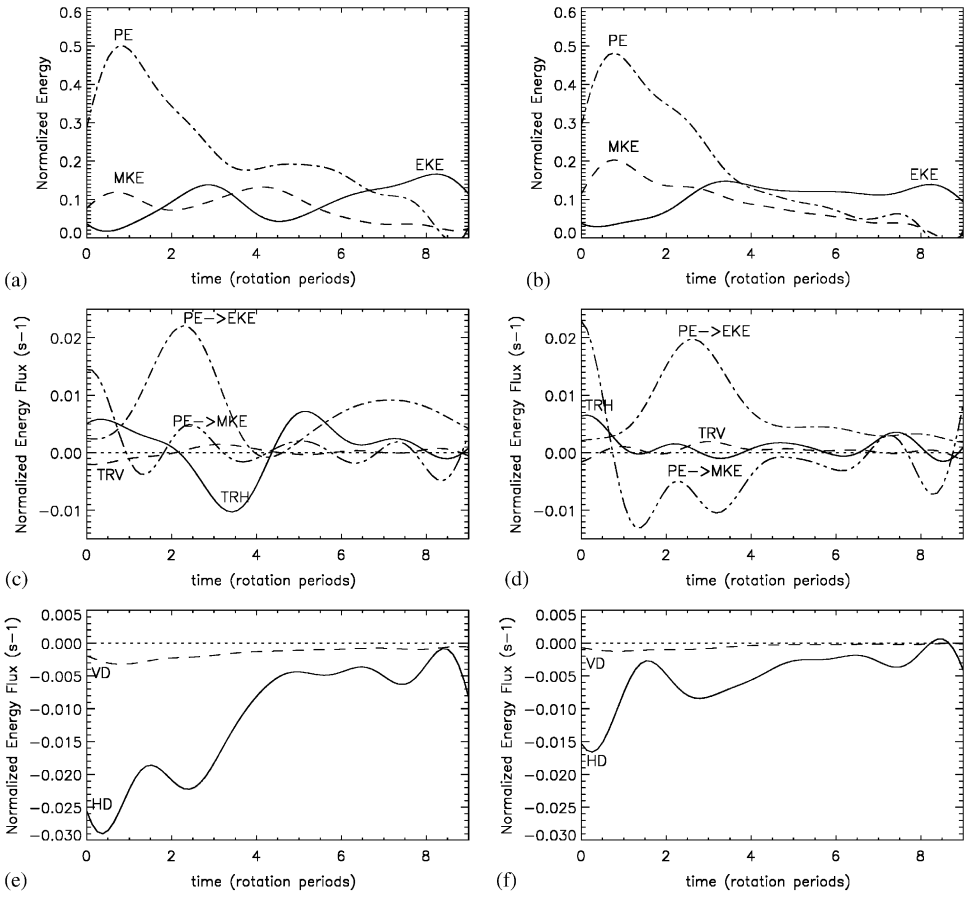

Fig. 8. (a) and (b) Temporal evolution of the eddy kinetic energy (EKE, solid line), the mean kinetic energy (MKE, dashed line) and the potential energy (PE, dash-dotted line). Open-ocean front is represented in (a) (run2.b) and coastal front in (b) (run4.b). (c) and (d) Temporal evolution of the main conversion terms of the EKE budget. PE $\rightarrow$ EKE (dash-dotted line) is the conversion of PE into EKE, the dominant process in baroclinic instability, TRH (solid line) is the conversion of MKE into EKE by horizontal Reynolds stresses acting on the horizontal gradient of the mean flow, TRV (dashed line) is the conversion of MKE into TKE by vertical Reynolds stresses acting on the vertical gradient of the mean flow. Open-ocean front is represented in (c) (run2.b) and coastal front in (d) (run4.b). (e) and (f) Temporal evolution of the dissipative terms of total kinetic energy. VD corresponds to vertical dissipation and HD to lateral dissipation. Note that these quantities have been normalized by $(\mathrm{PE}_{\max} - \mathrm{PE}_{\min})$, and filtered, for better visualization, using a low-pass filter ($f_c = 0.8f$).

transfer from the eddy motion to the mean flow as shown by the negative contribution of the barotropic energy-transfer term (see TRH) in Fig. 8c at $t \sim 3.5$ and by the increase in MKE (Fig. 8a). As a result of these transfers, two azimuthal jets developed. The radial shear of the inner jet is then strong enough to lead to the onset of barotropic instability (Fig. 8c at $t \sim 4.5$). Then baroclinic instability starts again at $t \sim 5$ (Figs. 6e and 8c) and eventually dominates while barotropic instability has stopped. Note that due to the wavy

pattern of the double front (Fig. 6f) it cannot be clearly seen whether baroclinic instability takes place only on the inner side or on both sides of the front. During the instability stage lateral dissipation of total kinetic energy dominates compared to vertical dissipation (Fig. 8e and f).

Finally, we compared these results for open-ocean fronts with those of Verzicco et al. (1997), hereafter V97. It is useful to stress that the dynamics in their study was mainly driven by the dimensionless number $Ri = ((R_d/R_c)^2)$[1] and the depth ratio. Similarly they observed that barotropic and baroclinic processes both came into play during the first stage of the instability. The time evolution of the energy-transfer terms of their run ($Ri = 0.09$) shows the four successive stages of baroclinic instability, eddy-mean flow interaction (TRH < 0 in Fig. 8c and in Fig. 17b of V97), barotropic instability (TRH > 0) and the second onset of baroclinic instability. However, this latest stage was not obtained in their run, $Ri = 0.2$ since the initial anticyclonic vortex was completely destroyed once dipoles had formed (see Fig. 9 of V97). Eddy dipoles could not organize themselves in order to reinforce significantly the mean flow as in Fig. 6d and e.

Near-coast fronts behave differently as soon as the baroclinic wave crest has reached the coast (Fig. 7a). The first difference with open-ocean fronts arises from the barotropic term which is never negative (Fig. 8d). Here, because of the presence of the coast, anticyclonic eddies cannot form. By contrast, the anticyclonic wave crest separates into two branches (Fig. 7b). The onshore upstream branch (UB; see Fig. 7b) flows along the coast while the offshore downstream branch (DB; see Fig. 7b) is deflected away from the coast due to the Coriolis force. This is in full agreement with the laboratory experiments (Chia et al., 1982; BA&L). In the laboratory experiments, cyclonic eddies were then advected offshore (BA&L). Basically the cyclonic eddies were enhanced at the coast, due to the upstream branch of the wave crest, and then advected by the downstream branch. By contrast, in the numerical simulations two behaviors are observed depending on the spatial organization of the wave. As seen in Fig. 7b, seven cyclonic eddies form at the coast, which corresponds to the most unstable baroclinic mode initially introduced. Then some of the eddies merge (Fig. 7c and d). Once they have merged they are advected offshore (Fig. 7d). In other cases, the scenario differs (Fig. 7e and f). The baroclinic wave is fairly asymmetric when it reaches the coast (Fig. 8e). Mode 5 dominates (though mode 7 had been introduced initially). Note that in this case (run2.b) the radius of the tank is 2 cm larger than that of run3.b. Therefore, the baroclinic wave reaches the coast at a later stage of evolution, for which nonlinear wave interactions have led to the growth of mode 5. Then the cyclonic eddy located in the lower part is advected offshore in a similar manner to that observed in the laboratory experiments (BA&L). Other eddies (the two in the upper left part of Fig. 7d) merge (Fig. 7e) before they are advected offshore as in run3.b. In conclusion, an asymmetry in the breaking wave is a necessary condition for offshore advection of cyclonic eddies to occur. In other words, the velocity in the offshore downstream branch needs to be greater than that of the onshore upstream branch. The opposite occurs in the backward-breaking baroclinic wave since the upstream branch is entrained by the cyclonic troughs. Therefore, while reaching the coast, there is no reason, if wave symmetry (pure mode) is preserved, for offshore advection to

[1] We have chosen W^2 in our simulations since we focused on the influence of the coast and kept Ri constant (from run0 to run4).

occur. In contrast the offshore downstream branch can "overcome" the onshore upstream branch if a less intense cyclonic eddy develops upstream. Let us call "A" the cyclonic eddy that is going to be advected and "B" the upstream less intense cyclonic eddy. The offshore downstream branch leading to offshore advection of A is mainly driven by the rolling process of B since it arises from the wave-crest separation at the coast. Since B is fairly weak the onshore upstream branch of the anticlyclonic wave which separates at the coast is weaker than the offshore downstream branch. Therefore, advection of A will occur.

Basically an offshore advection of cyclonic eddies was observed once the eddy had been enhanced along the coast in the case of an asymmetric baroclinic wave. In the laboratory experiments (BA&L), only this case was observed. Indeed, the baroclinic wave was never a pure mode and therefore the different crests were at different stages of development. Cyclonic eddies usually detached one by one. Very likely the other scenario—pure mode growth, eddy merging and offshore advection—is an artefact of the numerical simulations: it appears unlikely that such a symmetric wave would grow in the laboratory. By contrast, in numerical simulations, one has to "wait" until nonlinearities have become significant enough to break the initial symmetry of the flow.

In conclusion, we should stress the excellent agreement between laboratory experiments and numerical simulations. The main result of the laboratory experiments was that the growth of cyclonic eddies was enhanced compared to that of the anticyclonic vorticity as the front developed more and more near the coast (see Fig. 11 of BA&L). These values show an excellent agreement with the laboratory results (see Table 3). Eventually we have investigated the effect of the curvature of the coast on the intensification of cyclonic eddies. To this aim we have considered a cylinder with a wavy wall (run2.c). A value of 1.82 for the intensification is obtained which compares well with the 1.80 obtained in a cylindrical tank.

Table 3
Enhancement of cyclonic eddies relative to anticyclonic eddies: the ratio between the growth rate of the cyclonic vorticity and that of the anticyclonic vorticity, r, as a function of W^2

	W^2	δ	r
Numerical simulations			
run1.a	32.4	0.43	0.82
run1.b	32.4	0.71	0.86
run2.b	13.7	0.71	1.80
run2.c	13.7	0.71	1.82
run3.b	3	0.71	3.00
run4.a	1.7	0.43	2.95
run4.b	1.7	0.71	3.50
run5	4	0.66	4.04
Laboratory experiments			
	35	0.21	0.78
	25	0.63	1.09
	16	0.63	1.18
	8.3	0.74	1.85
	3.96	0.66	3.06
	2.2	0.19	3.25

All runs with $\delta = 0.71$ are shown here as well as two runs with $\delta = 0.43$, with some of the laboratory results.

4. Conclusion

This work was motivated by laboratory experiments on upwelling fronts (Chia et al., 1982; BA&L) which gave evidence of the striking effect of the coast on the growth of cyclonic eddies consisting of dense coastal water. We performed numerical simulations in order to better understand this process. First, new details of the adjustment process were gained. We showed that when the front is closer to the coast the release of potential energy is higher and that the radiated inertial waves are more energetic. A detailed investigation of the front instability showed that a dominant baroclinic instability occurred. For open-ocean fronts, eddy dipoles form during the latest stage of the initial baroclinic instability. These eddies then feed back to the mean flow, leading to a double jet. As a consequence of these energy transfers, the radial shear of the inner jet is strong enough to allow the onset of barotropic instability and the restart of baroclinic instability. By contrast, for coastal fronts, the enhancement of cyclonic eddies is observed at the coast in a manner similar to that observed in the laboratory experiments. Some differences regarding the offshore advection of cyclonic eddies when the baroclinic wave is fairly symmetric were observed, however. The eddies merged before being advected offshore. On the contrary, when the wave was highly asymmetric, cyclonic eddies were advected at once, as in the laboratory experiments. Eventually we duplicate in our simulations the main result of BA&L: the increase in the growth rate of cyclonic eddies when the front develops more and more close to the coast.

The follow-up of this study would be to investigate how exchanges of water masses are modified by the proximity to the coast. It seems that for open-ocean fronts the offshore transport would be weaker than for coastal fronts because, in the former case, eddies remain in the frontal region. By contrast the offshore advection of cyclonic eddies containing coastal water might lead to significant transport. This hypothesis can be tested in the numerical simulations by introducing a dye in coastal waters just after the adjustment of the front and by studying its further evolution. Another important feature which we did not take into account is the bottom topography. It is likely, if the bottom slopes strongly enough, that the instability will be modified. As already observed in laboratory experiments (Bouruet-Aubertot and Linden, 1999), cyclonic eddies have a tendency to remain in the slope region when bottom topography is introduced. Exchanges across the front should therefore be reduced.

Finally, it would be interesting to investigate the influence of the coast when the upwelling front forms in a different way. For instance, the evolution of an upwelling front produced by a constant surface stress, as that studied, for instance, by Ivey et al. (2000), could be considered. In this case, the role of the wind forcing in the dynamics of the front could be studied.

Acknowledgements

The simulations were performed on the NEC SX-5 of the Institut du Développement et des Ressources en Informatique Scientifique (IDRIS) under contract 227. We have benefited from the update and development of the code “Océan Parallélisé” (OPA) carried out by the Institut Pierre Simon Laplace (IPSL) and the Laboratoire d’Océanographie Dynamique et

Climatologie (LODYC). We thank Ray C. Griffiths for editing this manuscript. Vincent Echevin acknowledges the financial support from Service Hydrographique de la Marine (SHOM).

Appendix A

A.1. Energy budgets

The energy quantities and conversion terms are summarized in the following. Let us define the expressions $\bar{\alpha}(r,z) = 1/2\pi \int_0^{2\pi} \alpha(r,\theta,z)\,\mathrm{d}\theta$ and $\alpha'(r,\theta,z) = \alpha'(r,\theta,z) - \bar{\alpha}(r,z)$. With $\boldsymbol{U}_\mathrm{h}$ the horizontal velocity, we define,

$$\mathrm{MKE} = \int_V \tfrac{1}{2}(\bar{\boldsymbol{U}}_\mathrm{h})^2 r\,\mathrm{d}r\,\mathrm{d}\theta\,\mathrm{d}z \tag{A.1}$$

$$\mathrm{EKE} = \int_V \tfrac{1}{2}\overline{(\boldsymbol{U}'_\mathrm{h})^2} r\,\mathrm{d}r\,\mathrm{d}\theta\,\mathrm{d}z \tag{A.2}$$

$$\mathrm{PE} = \int_V \frac{1}{\rho_0}(\rho g z) r\,\mathrm{d}r\,\mathrm{d}\theta\,\mathrm{d}z \tag{A.3}$$

The temporal evolution equations of these energy quantities are:

$$\partial_t \mathrm{MKE} = -\mathrm{TRH} - \mathrm{TRV} + (\mathrm{PE} \to \mathrm{MKE}) - \mathrm{CENTR} + \overline{\mathrm{HD}} + \overline{\mathrm{VD}} \tag{A.4}$$

$$\partial_t \mathrm{EKE} = \mathrm{TRH} + \mathrm{TRV} + (\mathrm{PE} \to \mathrm{EKE}) + \mathrm{CENTR} + \mathrm{HD}' + \mathrm{VD}' \tag{A.5}$$

$$\partial_t \mathrm{PE} = -(\mathrm{PE} \to \mathrm{MKE}) - (\mathrm{PE} \to \mathrm{EKE}) + \mathrm{PED} \tag{A.6}$$

The conversion terms are listed in the following:

- TRH is the conversion of mean kinetic energy into eddy kinetic energy by horizontal Reynolds stresses acting on the horizontal shear of the mean flow:

$$\mathrm{TRH} = \int_V \overline{u'_r u'_r}\,\partial_r(\overline{u}_r) r\,\mathrm{d}r\,\mathrm{d}\theta\,\mathrm{d}z + \int_V \overline{u'_r u'_\theta}\,\partial_r(\overline{u_\theta}) r\,\mathrm{d}r\,\mathrm{d}\theta\,\mathrm{d}z \tag{A.7}$$

- TRV is the conversion of MKE into EKE by vertical Reynolds stresses acting on the vertical shear of the mean flow:

$$\mathrm{TRV} = \int_V \overline{u'_r w'}\,\partial_z(\overline{u_r}) r\,\mathrm{d}r\,\mathrm{d}\theta\,\mathrm{d}z + \int_V \overline{u'_\theta w'}\,\partial_z(\overline{u_\theta}) r\,\mathrm{d}r\,\mathrm{d}\theta\,\mathrm{d}z \tag{A.8}$$

- CENTR is the conversion of MKE into EKE by centrifugal forces:

$$\mathrm{CENTR} = \int_V \overline{u'_r u'_\theta}(\overline{u_\theta})\,\mathrm{d}r\,\mathrm{d}\theta\,\mathrm{d}z - \int_V \overline{u'_\theta u'_\theta}(\overline{u_r})\,\mathrm{d}r\,\mathrm{d}\theta\,\mathrm{d}z \tag{A.9}$$

- PE→EKE is the conversion of potential energy into eddy kinetic energy by baroclinic instability processes:

$$(\mathrm{PE} \to \mathrm{EKE}) = -\int_V \frac{1}{\rho_0} g\overline{\rho' w'} r\,\mathrm{d}r\,\mathrm{d}\theta\,\mathrm{d}z \tag{A.10}$$

- PE→MKE is the conversion of potential energy into mean kinetic energy:

$$(\mathrm{PE} \rightarrow \mathrm{MKE}) = -\int_V \frac{1}{\rho_0} g\bar{\rho}.\bar{w}r \,\mathrm{d}r \,\mathrm{d}\theta \,\mathrm{d}z \tag{A.11}$$

- The dissipation term can be splitted into horizontal dissipation (HD) and vertical dissipation (VD):

$$\mathrm{HD} = \int_V \overline{D_\mathrm{h}(\boldsymbol{U}'_\mathrm{h})\boldsymbol{U}'_\mathrm{h}} r \,\mathrm{d}r \,\mathrm{d}\theta \,\mathrm{d}z + \int_V D_\mathrm{h}(\bar{\boldsymbol{U}}_\mathrm{h})\bar{\boldsymbol{U}}_\mathrm{h} r \,\mathrm{d}r \,\mathrm{d}\theta \,\mathrm{d}z = \mathrm{HD}' + \overline{\mathrm{HD}} \tag{A.12}$$

$$\mathrm{VD} = \int_V \overline{D_\mathrm{v}(\boldsymbol{U}'_\mathrm{h})\boldsymbol{U}'_\mathrm{h}} r \,\mathrm{d}r \,\mathrm{d}\theta \,\mathrm{d}z + \int_V D_\mathrm{v}(\bar{\boldsymbol{U}}_\mathrm{h})\bar{\boldsymbol{U}}_\mathrm{h} r \,\mathrm{d}r \,\mathrm{d}\theta \,\mathrm{d}z = \mathrm{VD}' + \overline{\mathrm{VD}} \tag{A.13}$$

- The term noted PED can be split into the horizontal diffusion term (PEHD), vertical diffusion (PEVD, a source term) and a convective adjustment term (PECONV, a sink term):

$$\mathrm{PED} = \int_V \frac{1}{\rho_0} gz[D_\mathrm{h}(\rho) + K_z \partial^2_{zz}(\rho) + \frac{1}{\rho_0} gz(\rho - \rho_{\mathrm{static}})] r \,\mathrm{d}r \,\mathrm{d}\theta \,\mathrm{d}z \tag{A.14}$$

$$\mathrm{PED} = \mathrm{PEHD} + \mathrm{PEVD} + \mathrm{PECONV} \tag{A.15}$$

Because of the model cartesian grid, density and velocity fields were interpolated off-line onto a cylindrical grid from model outputs every 50 time steps. Energy and conversion terms were calculated on the cylindrical grid, except for HD′, VD′, $\overline{\mathrm{HD}}$ and $\overline{\mathrm{VD}}$. For the latter terms, only HD and VD, calculated on-line for every model time step, are shown in Fig. 8, PED was not shown since it is weak compared to the other terms of Eq. (A.6).

References

Bouruet-Aubertot, P., Linden, P.F., 1999. Laboratory experiments on upwelling fronts. In: Proceedings of the European Geophysical Society Meeting, Den Haag.

Bouruet-Aubertot, P., Linden, P.F., 2002. The influence of the coast on the dynamics of upwelling fronts. Part I. Laboratory experiments. Dyn. Atmos. Oceans 36 (1–3), 153–173.

Chia, F., Griffiths, R.W., Linden, P.F., 1982. Laboratory experiments on fronts. Part 2. The formation of cyclonic eddies at upwelling fronts. J. Geophys. Astrophys. Fluid Dyn. 19, 189–206.

Crépon, M., Wald, L., Monget, J.L., 1981. Low-frequency waves in the Ligurian Sea during December 1977. J. Geophys. Res. 87, 595–600.

Cushman-Roisin, B., Heil, W.H., Nof, D., 1985. Oscillations and rotations of elliptical warm-core rings. J. Geophys. Res. 90, 64.

Gill, A.E., 1982. Atmosphere–Ocean Dynamics. Academic Press, London, 662 pp.

Griffiths, R.W., Linden, P.F., 1981a. The stability of vortices in a rotating stratified fluid. J. Fluid Dyn. 105, 283–316.

Griffiths, R.W., Linden, P.F., 1981b. The stability of buoyancy-driven coastal currents. Dyn. Atmos. Oceans 5, 281–306.

Griffiths, R.W., Linden, P.F., 1982. Laboratory experiments on fronts. Part I. Density-driven boundary currents. J. Geophys. Astrophys. Fluid Dyn. 19, 159–187.

Holford, J.M., 1994. The evolution of a front. Ph.D. thesis, DAMTP, Cambridge University.

Holford, J.M., Dalziel, S.B., 1996. Measurements of layer depth during baroclinic instability of a two-layer flow. Appl. Sci. Res. 56, 191–207.

Ivey, G.N., Winters, K.B., Coates, M.J., 2000. Modelling upwelling in the coastal ocean. In: Lawrence, G.A., Pieters, R., Yonemitsu, N. (Eds.), Proceedings of the Stratified Flows Conference, Vancouver, pp. 679–684.

Kunze, E., 1985. Near-inertial wave propagation in geostrophic shear. J. Phys. Oceanogr. 15, 545–565.

Madec, G., Delecluse, P., Imbard, M., Levy, C., 1998. OPA8.1 Ocean General Circulation Model Reference Manual, Note 11. Institut Pierre Simon Laplace, Paris, 91 pp.

Narimousa, S., Maxworthy, T., 1985. Two-layer model of shear-driven coastal upwelling in the presence of bottom topography. J. Fluid Dyn. 159, 503–531.

Narimousa, S., Maxworthy, T., 1987. Coastal upwelling on a sloping bottom: the formation of plumes, jets and pinched-off cyclones. J. Fluid Dyn. 176, 169–190.

Roullet, G., Madec, G., 2000. Salt conservation, free surface and varying volume: a new formulation for Ocean GCMs. J. Geophys. Res. 105 (23), 927–942.

Smolarkiewicz, K.P., Clark, T.L., 1986. The multidimensional positive definite advection transport algorithm: further development and applications. J. Comput. Phys. 67, 396–438.

Verzicco, R., Lalli, F., Canoaram, E., 1997. Dynamics of baroclinic vortices in a rotating, stratified fluid: a numerical study. Phys. Fluids 9 (2), 419–432.